An X-ray Investigation of Three Supernova Remnants in the Large Magellanic Cloud

Matthew Klimek

NOAO/CTIO REU/Rutgers University

klimek@eden.rutgers.edu

and

S. D. Points, C. Smith

Cerro Tololo Inter-American Observatory

points@ctio.noao.edu, chris@ctio.noao.edu

Received _____; accepted _____

ABSTRACT

The Large Magellanic Cloud (LMC), with its low foreground absorption and proximity, offers the ideal site to study a large sample of supernova remnants (SNRs) in detail, both spatially and energetically. It is possible to obtain a relatively complete sample of SNRs in the LMC to examine both global properties and the subclasses of SNRs. Toward this goal, we have identified new SNRs using multi-wavelength data. The newly recognized SNRs are generally fainter than the known sample, and may represent a previously missed population.

We have obtained X-ray images and spectra of three of these recently identified SNRs using the *XMM-Newton* observatory. These data, in conjunction with pre-existing optical emission-line images and spectra and radio continuum data, are used to determine the physical conditions of the warm (10^4 K) ionized gas and the hot (10^6 K) ionized gas. We compare the morphologies of the SNRs in the different waveband. The physical properties of the warm ionized shell are determined from the Hα surface brightness and the SNR expansion velocity. The X-ray spectra were fit with a Raymond-Smith thermal plasma model and the physical conditions of the hot gas are derived from the model fits. We find that the pressure of the hot gas is greater than that in the warm shell by about an order of magnitude, implying that these remnants are in the pressure-driven expansion stage. We also discuss the ages and classifications of the remnants.

Subject headings:

1. Introduction

Supernovae (SNe) and their remnants are the driving force behind the dynamic interstellar medium (ISM) of our Galaxy and others. The study of the energetics and evolution of supernova remnants (SNRs) thus forms the foundation for developing a complete understanding of the complex structure and evolution of the ISM in most galaxies. However, in order to form an accurate picture of how SNRs influence the ISM, it is necessary to have a complete and unbiased sample of SNRs in a galaxy. This is very difficult within the Milky Way as dust absorption and confusion along the line-of-sight hinders our ability to detect and determine the physical conditions of galactic SNRs. although it is possible to obtain a more complete sample of SNRs in more distant galaxies, their distance hinders the investigation of their physical conditions in detail.

The Large Magellanic Cloud (LMC) offers the ideal laboratory for the study of a large sample of SNRs. The LMC is well out of the galactic plane and thus offers low foreground absorption ($A_v \sim 0.3$)[cite]. Meanwhile, its distance is relatively well known ($\sim$50 kpc; Feast 1999) and distances within the LMC are small compared with its distance to us so all objects within the LMC can be taken to be at the same distance. Its proximity also allows us to resolve a great amount of spatial detail (1"$\approx$ 0.25 pc).

The canonical sample of 32 SNRs in the LMC (Mathewson et al. 1983, 1984, 1985) was woefully incomplete (*e.g.,* Helfand 1984), and heavily biased to remnants that are bright at one or more wavelengths. The SNRs presented in this paper were discovered as regions of shock-ionized gas in the Magellanic Cloud Emission Line Survey (MCELS). New X-ray data have been obtained from the *XMM-Newton* observatory and analyzed along with the optical data from MCELS and radio data from the Australia Telescope Compact Array (ATCA) to form a complete picture of these SNRs.

Below, Section 2 presents the three sets of observations upon which this study is based.

Section 3 describes the three SNRs. Their physical properties and their derivation are discussed in Section 4.

2. Observations

2.1. Optical Emission-line Data

MCELS was undertaken to provide an atlas of diffuse features in the interstellar medium of our nearest neighbor galaxies the Large and Small Magellanic Clouds (LMC and SMC, respectively). Deep observations were taken of the LMC and SMC in [O III] ($\lambda_c = 5007$Å, FWHM = 40Å), Hα ($\lambda_c = 6563$Å, FWHM = 30Å), and [S II] ($\lambda_c = 6724$Å, FWHM = 50Å) emission lines with the UM/CTIO Heber D. Curtis Schmidt telescope at Cerro Tololo Inter-American Observatory (CTIO). The detector was a thinned, back-side illuminated Tek 2048 × 2048 CCD with 24μm pixels, giving a $1.^\circ3 \times 1.^\circ3$ field-of-view with a scale of $2.''3$ pixel^{-1} and resulting angular resolution of $\sim 4.''6$. Continuum images in the green ($\lambda_c = 5130$Å, FWHM = 155Å) and red ($\lambda_c = 6850$Å, FWHM = 95Å) bands were taken to aid in the subtraction of non-emission line sources. Two slightly offset images were taken through each filter to allow rejection of cosmic rays and bad pixels. The total integration times were 1200 s in the [O III] and [S II] images and 600 s in the Hα, green, and red images.

These data were reduced using the IRAF[1] software package. Bias subtraction and flat-field corrections were applied. The data were filtered for cosmic ray events and bad pixels. The images were then normalized to a one second exposure and a constant sky level was determined from the peak of the histogram of pixel values and subtracted. The images were also scaled to a pixel size of 2" and aligned to a WCS grid based on the HST

[1]IRAF is distributed by the National Optical Astronomy Observatories (NOAO).

Guide Star and USNO-A catalogs using an automated WCS routine based on code from Brian Schmidt and IRAF routines. Next, the data were calibrated to convert pixel values from ADUs to surface brightness using data from whoever (whenever). Corresponding exposures were then combined. Each emission line image contains emission from that atomic transition as well as a contribution from the continuum. In order to correct for the continuum contribution to the flux observed at the emission line frequency, we chose several stars in the continuum exposures, measured their flux and found the factor to scale their continuum flux to their flux in the emission line image. The continuum images were scaled by this factor and subtracted from the emission line images. The MCELS images of these SNRs are presented in Figure 1.

The ratio of [S II]/Hα is an effective discriminant between SNRs and photoionized regions (such as the ubiquitous H II regions; see Figure 2) since typical SNRs have ratios between 0.4 and 1, while photoionized regions usually exhibit much lower ratios of order 0.1. To aid in identification of previously unknown shock-ionized regions, the continuum-subtracted Hα and [S II] images were divided. Shocked features stand out clearly from nearby H II regions in these images. See Figure 3 for Hα/[S II] maps of the SNRs presented in this study.

2.2. X-ray Data

This study presents new X-ray data from *XMM-Newton* (Proposal Numbers 20526 and 30141). Proposed pointings were chosen to follow up on regions of high [S II]/Hα from the MCELS data. Four observations were awarded, three of which are presented in this paper (Observation Numbers 205260101, 205260201, and 301410601).

These data were processed with the *XMM-Newton* Science Analysis Software[2] (SAS) package. Data from *XMM-Newton* European Photon Imaging Camera Metal Oxide Semiconductor (EPIC MOS) detectors were initially processed with the EMCHAIN sequence in SAS. Light curves for the entire exposure were extracted and visually inspected for periods of high background contamination. Nominal good count rates were about $\sim$1 s^{-1}. The high background periods were removed and the good data were filtered for poor event grades (see Figures 4 and 5). Spectra were extracted from the regions of interest, as well as from source-free regions for purposes of background subtraction.

For visual inspection, adaptively smoothed images were created with the Extended Source Analysis Software (ESAS) package. ESAS is a package of perl scripts which call SAS commands and standalone fortran programs following analysis techniques given by Snowden and Kuntz (2006). Two sets of images were made with event energies restricted to the ranges 0.35-1.25 keV and 2.0-8.0 keV. This choice was motivated by the fact that a thermal plasma emits primarily in the lower energy band, while the higher energy band allows us to search for point source emission. We present the smoothed X-ray images in Figure 6.

2.3. Radio Data

To complete our investigation, we obtained the 4.8 GHz and 8.6 GHz radio mosaics of the LMC from Dickel et al. (2005) taken with the Australia Telescope Compact Array (ATCA). The mosaics consist of 7085 individual points which together cover 6^o on a side.

[2]The *XMM-Newton* SAS is developed and maintained by the Science Operations Centre at the European Space Astronomy Centre (ESAC), Madrid, Spain and the Survey Science Centre at the University of Leicester, Leicester, UK.

These data have a half-power beam width of 33" which provides a spatial resolution of 8 pc at the distance of the LMC. While these data lack the angular resolution of the optical and x-ray data, they are sufficient to support our conclusions about the structure of these SNRs.

Individual pointings were calibrated, edited, and cleaned by standard MIRIAD processes before being combined into the mosaic. Bright structures in the area of 30 Doradus produced strong sidelobe structures. Some archival data from ATCA was added in order to improve signal-to-noise ratios in this area. A more comprehensive discussion of these data, their reduction, and analysis are given in Dickel et al. (2005). We present the radio images in Figure 7.

3. Description of Individual Objects

In this study, I use the X-ray morphology classification system defined by Williams (1999).

3.1. SNR0449−6921

SNR0449−6921 shows the simplest structure of the three remnants presented here. It lies on the edge of a large H II region, but a well defined shell structure is visible in the optical data. Contained within this optical shell is a smooth distribution of soft X-ray emission. This matches the shell-type supernova classification from Williams. The entire area of the neighboring H II region is diffused with radio emission and it is thus difficult to distinguish radio emission from the remnant itself from emission associated with the H II cloud. [Check this]

3.2. SNR0506−6541

SNR0506−6541 shows a clear shell structure in the optical data, however the shell is not a clean sphere as in SNR0449−6921. The southwestern edge shows a bright flat region with complex filamentary structure. There appears to be a gap in the shell along the southern edge but closer investigation shows faint optical filaments extending southwestward and reconnecting with the flat region mentioned above. The [O III] image displays complex filamentary structure inside the shell which is less apparent in the Hα and [S II] images. The shell is filled with diffuse soft X-ray emission but it is not as evenly distributed as in SNR0449−6921. X-ray contours reveal gaps in the emission and several local maxima. For this reason I classify SNR0506−6541 as a diffuse-face type remnant. X-ray emission extends into the bubble on the south side of the remnant but is completely contained by the faint optical filaments. The radio image also shows emission filling the shell at levels noticeably higher than the background.

3.3. SNR0537−6628

SNR0537−6628 also lies on the edge of an H II region. Optical filaments are visible but they do not lie in a clear shell-like pattern. Also, along the western edge, closest to the H II region, it is difficult to distiguish between H II clouds and the optical shells of the remnant. Whether these western filaments are part of the remnant is further obscured by the fact that X-ray emission is confined to the eastern part of this region. X-ray emission is for the most part confined by the other filaments on the eastern side of the remnant although it appears that there may be a few small break-outs as trails of X-ray emission are visible extending east and south from the remnant. The X-ray emission is smoothly distributed and matches the shell-like classification. There is one gap in the X-ray emission in the center of the remnant, but I attribute this to absorption by a foreground hydrogen

cloud. As in SNR0449−6921 the close proximity of the H II region confuses identification of radio emission associated with the SNR.

4. Discussion

4.1. Warm ionized shell (10^4 K)

Using the flux-calibrated MCELS images, we measured an Hα surface brightness. The images have been scaled such that each pixel corresponds to 0.25 pc in the LMC. With this, we measure the average radius of the shell and its thickness. We assume a standard ISM radiation field such that helium is singly ionized so that $n_e = 1.1 n_H$. Given a shell thickness ΔR, the line of sight through the shell is

$$\mathcal{L} = 2\sqrt{R^2 - (R - \Delta R)^2}$$

The emission measure of the warm gas $EM = n_e^2 \mathcal{L}$ is related to the surface brightness by [cite]

$$EM = SB \times 5 \times 10^{17} \Longrightarrow n_e = \Big(\frac{SB \cdot 5 \times 10^{17}}{\mathcal{L}}\Big)^{1/2}$$

Assuming $n_{He}/n_H = 0.1$ the density of massive particles (protons and neutrons) is given by

$$n_{pn} = n_H + 4n_{He} = n_H + 0.4 n_H = 1.27 n_e$$

Thus the total mass of the warm ionized shell is

$$M_{wig} = n_{pn} m_p f_{wig} V_{shell}$$

where f_{wig} is a filling factor between 0 and 1 and

$$V_{shell} = \frac{4}{3}\pi(R^3 - (R - \Delta R)^3)$$

Expansion velocities have been determined from echelle spectra of the Hα emission-line, and thus we may determine kinetic energies for the warm shells by

$$K = \frac{1}{2} M_{wig} v_{exp}^2$$

We may also determine the age of the SNR with the expansion velocity by the relation

$$t_{age} = \eta R / v_{exp}$$

given the factor η which depends upon the physics of the expanding shell. If we assume that $T_{wig} = 10^4$ K, we can also calculate the pressure in the shell:

$$P_{shell} = 2 n_e k T_{wig} = 2.76 \times 10^{-12} n_e$$

We present the results of our optical analysis of these SNRs in Table 2.

4.2. Hot ionized gas (10^6 K)

Regions extracted for spectral analysis as well as corresponding source-free background regions are presented in Figure ?. Based on the assumption that emission from the hot gas is predominantly thermal, we attempted fits with a Raymond-Smith (1977) thermal plasma model ("raymond" in XSPEC[3]). To this, we combined a power law component ("powerlaw" in XSPEC) to better fit the high energy tail from the hard X-ray extragalactic background. These are multiplied by a Wisconsin photoelectric absorption component ("wabs" in XSPEC). We also add an "apec" model component to account for hot plasma emission in the local hot bubble [ref].

[3]Details and references for all models used in this study can be found at http://heasarc.gsfc.nasa.gov/docs/xanadu/xspec/manual/manual.html.

Parameters for the Raymond-Smith model are the plasma temperature kT, interstellar abundances which we fix at 0.3 of solar, and a normalization constant $A = 10^{-14} \int n_e n_H dV / 4\pi D^2$. Here, n_e and n_H are the electron and hydrogen densities respectively, V is the volume occupied by the hot gas, and D is the distance to the remnant, in cgs units. The "apec" model is used with a fixed temperature $kT = 0.1$ keV (*cf.* Snowden and Kuntz, 2006) and solar abundances. It is fit for a normalization factor identical to that of the Raymond-Smith component. The power law component is allowed to vary in photon index and normalization. The absorption component has one parameter, hydrogen column density N_H, which is allowed to vary. To further constrain our X-ray spectral fits, we also used data from the ATCA 21-cm H I emission-line survey of the LMC (Kim et al.) to fix the H I column density.

Again we assume $n_{He}/n_H = 0.1$, but we now assume fully ionized helium such that $n_e = 1.2 n_H$. Given the thermal plasma normalization A we can calculate the electron density in the hot gas by

$$n_e = 3.89 \times 10^7 D \sqrt{A/V_{hot}} f_{hot}^{-1/2} = n_{ef} f_{hot}^{-1/2}$$

where V_{hot} is the volume of the hot gas. We use the radius to the inside edge of the warm shell and assume spherical symmetry to calculate V_{hot}. We leave our results in terms of f_{hot}. Massive particle density is again given by $n_{pn} = 1.17 n_e$ and so the mass of the hot gas is

$$M_{hot} = n_{pn} m_p V_{hot} f_{hot} = 1.17 n_{ef} m_p V_{hot} f_{hot}^{1/2}$$

To find the thermal energy we first need to know the total particle density, which is just

$$n = n_e + 1.1 n_H = 1.92 n_{ef} f_{hot}^{-1/2}$$

Now given the temperature from our spectral fits, the total thermal energy is then

$$E = \frac{3}{2} N k T = \frac{3}{2} n V_{hot} f_{hot} k T = 4.60 \times 10^{-9} n_{ef} V_{hot} T(keV) f_{hot}^{1/2}$$

We can also find that the pressure is

$$P_{hot} = nkT = 3.05 \times 10^{-9} n_{ef} T(kev) f_{hot}^{-1/2}$$

The results of our X-ray analysis of these SNRs are presented in Table 2.

4.3. Age Determination

The age of the SNR can be determined by the present radius of the shell, the velocity of the shell as determined by echelle spectra, and a factor η which accounts for the evolution of the expansion rate over the lifetime of the SNR. These factors are related to the age τ by

$$\tau = \eta R / v_{exp}$$

The expansion factor η depends upon the physical conditions of the SNR. For all three of these SNRs we find that the pressure of the internal hot ionized gas dominates that of the warm ionized shell by an order of magnitude, even for a filling factor of 1. If we assume that this pressure difference is the primary force driving the expansion, we can choose $\eta = 0.33$. (Osterbrock) This gives the ages which we present in Table 2.

5. Summary and Conclusions

5.1. Individual SNRs

The SNR J0449-6921 in N79 has a projected boundary overlapping the ring nebula around the WR star Br2. This ring nebula is unusual in its bright nebular HeIIλ4686 line emission, indicating a very high excitation (Garnett & Chu 1994). Two other examples of HeII-emitting nebulae are known in the LMC: the HeII nebula around the HMXB LMC X-1 (Pakull & Angibault 1986) and N44C which has been suggested to be ionized by the

transient LMC X-5 (Pakull & Motch 1989). It is not clear whether the SNR candidate is responsible for the high excitation of the ring nebula around Br2, either by direct dynamic interaction or by high-energy radiation flux from an X-ray binary. A high-resolution X-ray image of the SNR candidate and the WR ring nebula in N79 may reveal their relationship, possibly showing either X-ray emission at the SNR/WR wind interaction region or a point source either in the SNR or even possibly Br2 (if Br2 is itself the power for the nebular HeII).

SNR J0506-6541 (DEM 72), having a diameter of ∼75 pc (or 5′), would be the second largest isolated SNR in the LMC, larger than any known, clean-cut SNRs in our Galaxy. SNRs of such large sizes represent an advanced evolutionary stage, at which SNRs start to merge into the ISM. It is quite uncertain whether such evolved SNRs still contain hot gas in their interior (Slavin & Cox 1992). The largest SNR in the LMC (0450-70.9, 100×75 pc) has an upper limit of $< 2 \times 10^{35}$ ergs s^{-1} on its X-ray luminosity (Mathewson et al. 1985). J0506-6541, being smaller albeit still large, presents the most promising target for an X-ray study of hot interiors of evolved SNRs.

5.2. Future Work

In order to aid further searches SNRs in the LMC, future work could include a statistical analysis of the SNRs presented here against the previously-known population to determine why they were not discovered earlier. This knowledge could help guide future surveys.

Future work could also include extension of this study to the cool non-ionized shell of swept-up ISM material surrounding the warm shell. This will provide further insights into the energetics of the SNR and its environment.

As is always a problem with the study of diffuse structures, the physical properties are very dependent on the value of the filling factor f. Previous SNR studies have settled on chosen to use various values for f based upon models of SNR expansion. Future work could search for the model best suited to these remnants and thus suggest an appropriate value of f.

X-ray spectra could also be fitted for elemental abundances which would assist in the determination of the type of these SNRs.

MDK would like to extend his thanks to SDP and CS for their support and encouragement and the great amount of experience gained through this work. MDK also thanks NOAO/CTIO for the opportunity afforded by their REU program and to NSF for their funding of the REU.

REFERENCES

Smith et al. 2006

This manuscript was prepared with the AAS LaTeX macros v5.2.

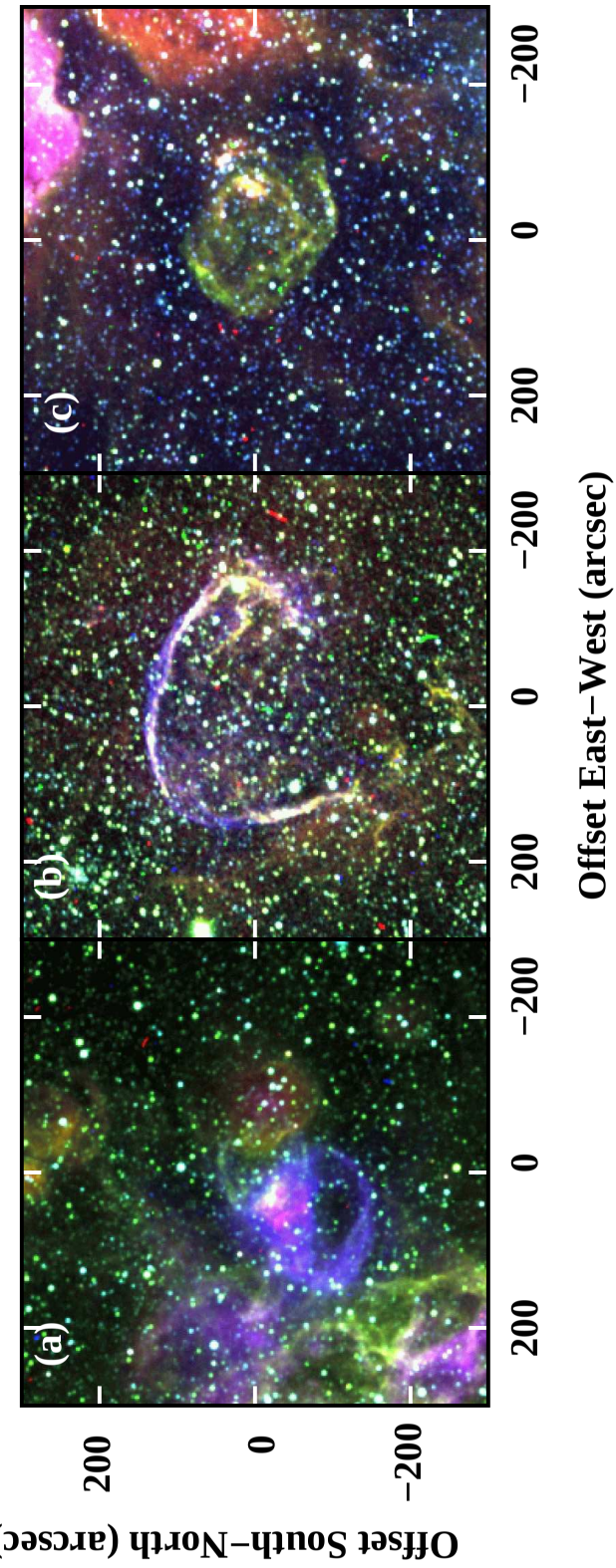

Fig. 1.— Three-color images of the SNRs using the MCELS data **(a)** J0449−6921, **(b)** J0506−6541, and **(c)** J0537−6628 with Hα - red, [S II] - green, [O III] - blue.

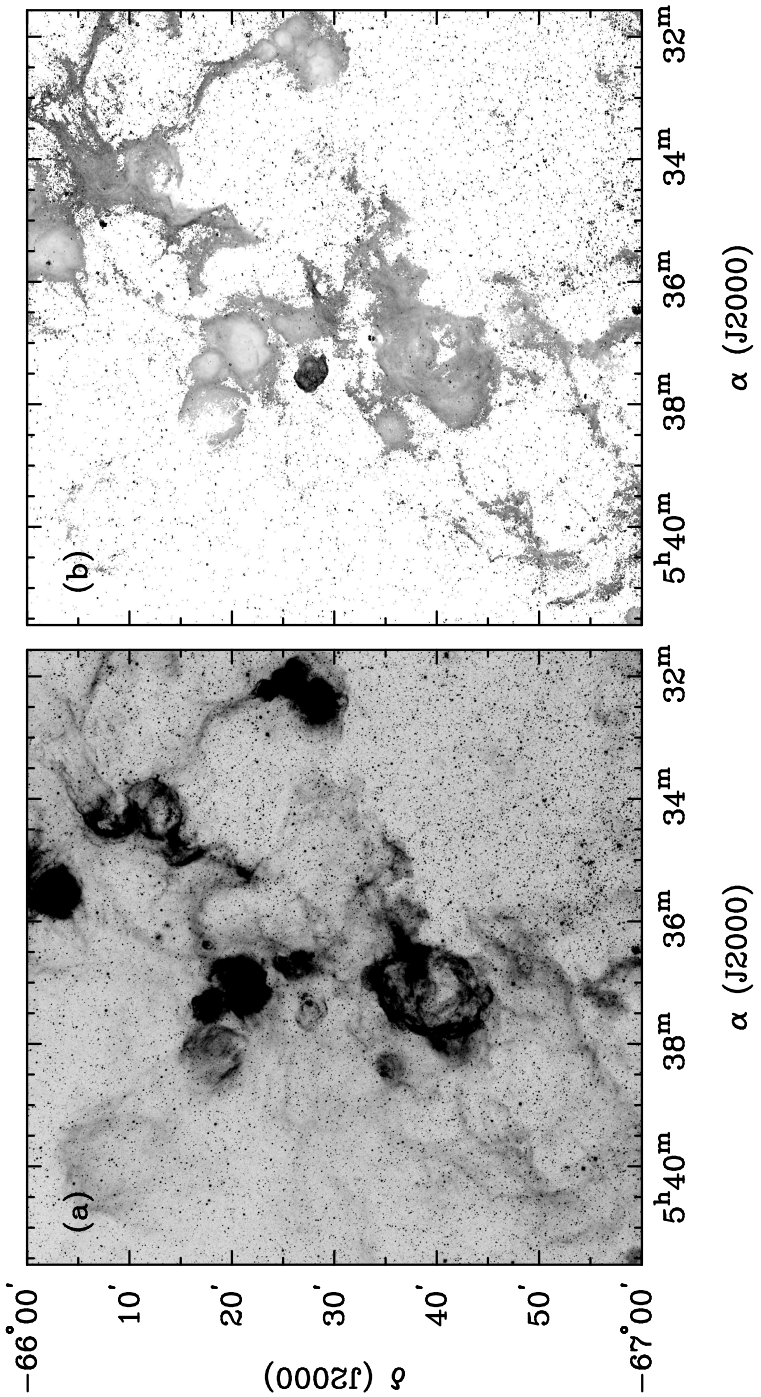

Fig. 2.— (a) An example of a full field Hα image, field LMC [-4, 4], from the MCELS project. The image is 1.2×1.2 degrees, and probes the Hα emission down to approximately $\sim 1 \times 10^{-17}$ erg cm^{-2} s^{-1} arcsec^{-2}, just below the diffuse Hα emission that Kennicutt et al. found in their extremely low resolution Hα image of the LMC. (b) An example of a full field [S II]/Hα ratio image from MCELS, showing the variations seen in these complex images. An SNR stands out clearly as the darker region in the center of the region.

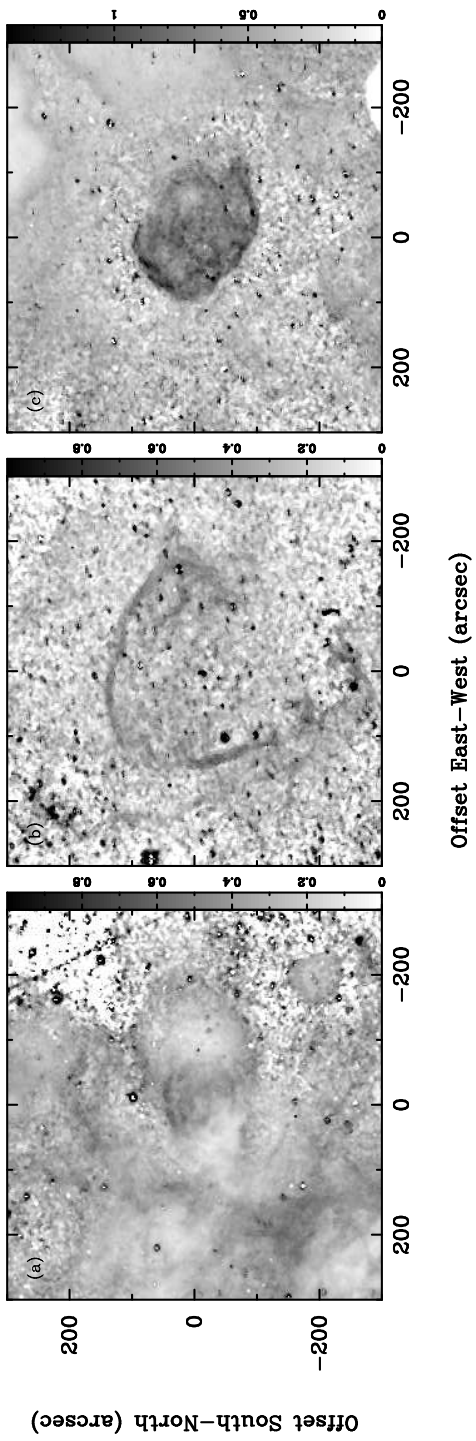

Fig. 3.— [S II]/Hα ratio maps for the three SNRs, **(a)** J0449−6921, **(b)** J0506−6541, and **(c)** J0537−6628 using the flux-calibrated MCELS [S II] and Hα images. The image intensity scales for each of the SNRs are displayed to the right of each image. The intensity scales range from 0 to 1 for all of the images except J0537−6628 which ranges from 0 to 1.4.

Fit Limits: Blue
Selection Limits: Red
3
4
5
t Rate (counts/s)
OV Light Curve

nt Rate Histogram
Fit Limits: Blue
Selection Limits: Red
3
4
5
nt Rate (counts/s)
0V Light Curve

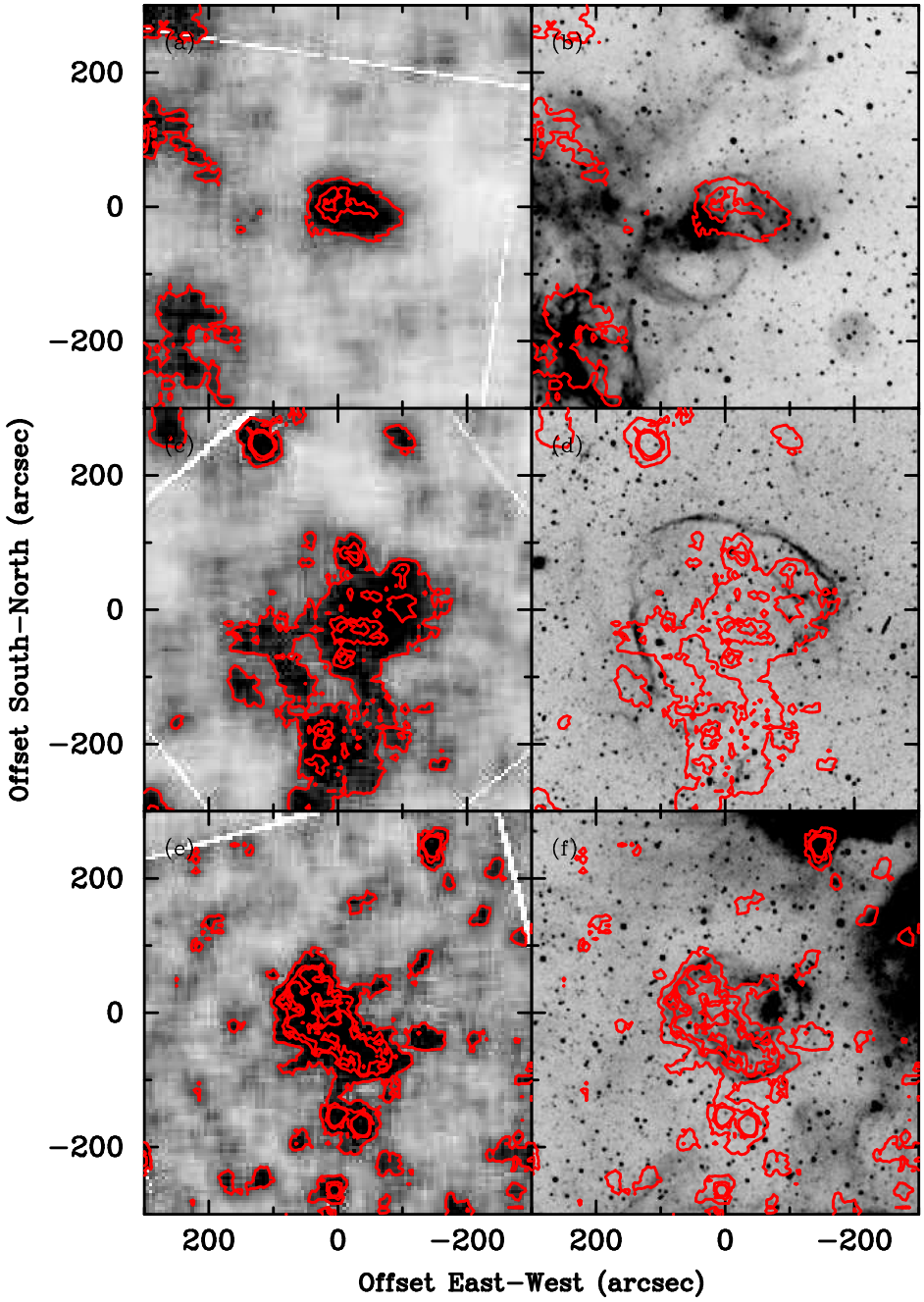

Fig. 6.— Mosaicked *XMM-Newton* EPIC MOS (left column) and MCELS Hα images (right column) of the SNRs overlaid with X-ray contours. **(a,b)** SNR J0449−6921, **(c,d)** SNR J0506−6541, and **(e,f)** SNR J0537−6628. The X-ray images are in the 0.35–1.25 keV energy band. The contour levels are 5, 10, and 15 counts s^{-1} $degree^{-2}$.

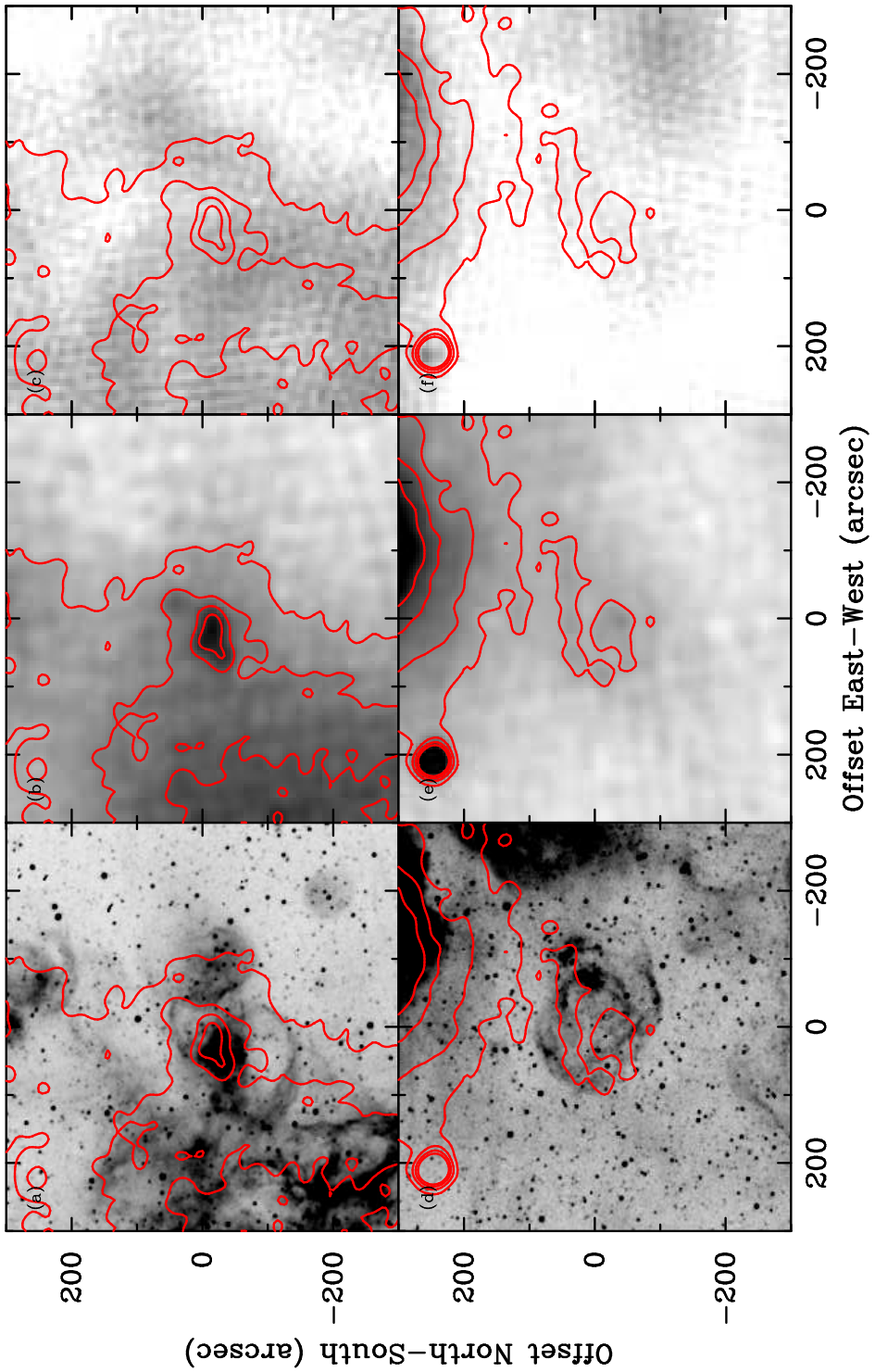

Fig. 7.— Mosaicked ATCA 4.8-GHz (left column) and MCELS Hα images (right column) of the SNRs overlaid with radio contours. **(a,b)** SNR J0449−6921, **(c,d)** SNR J0506−6541, and **(e,f)** SNR J0537−6628. The contour levels are .

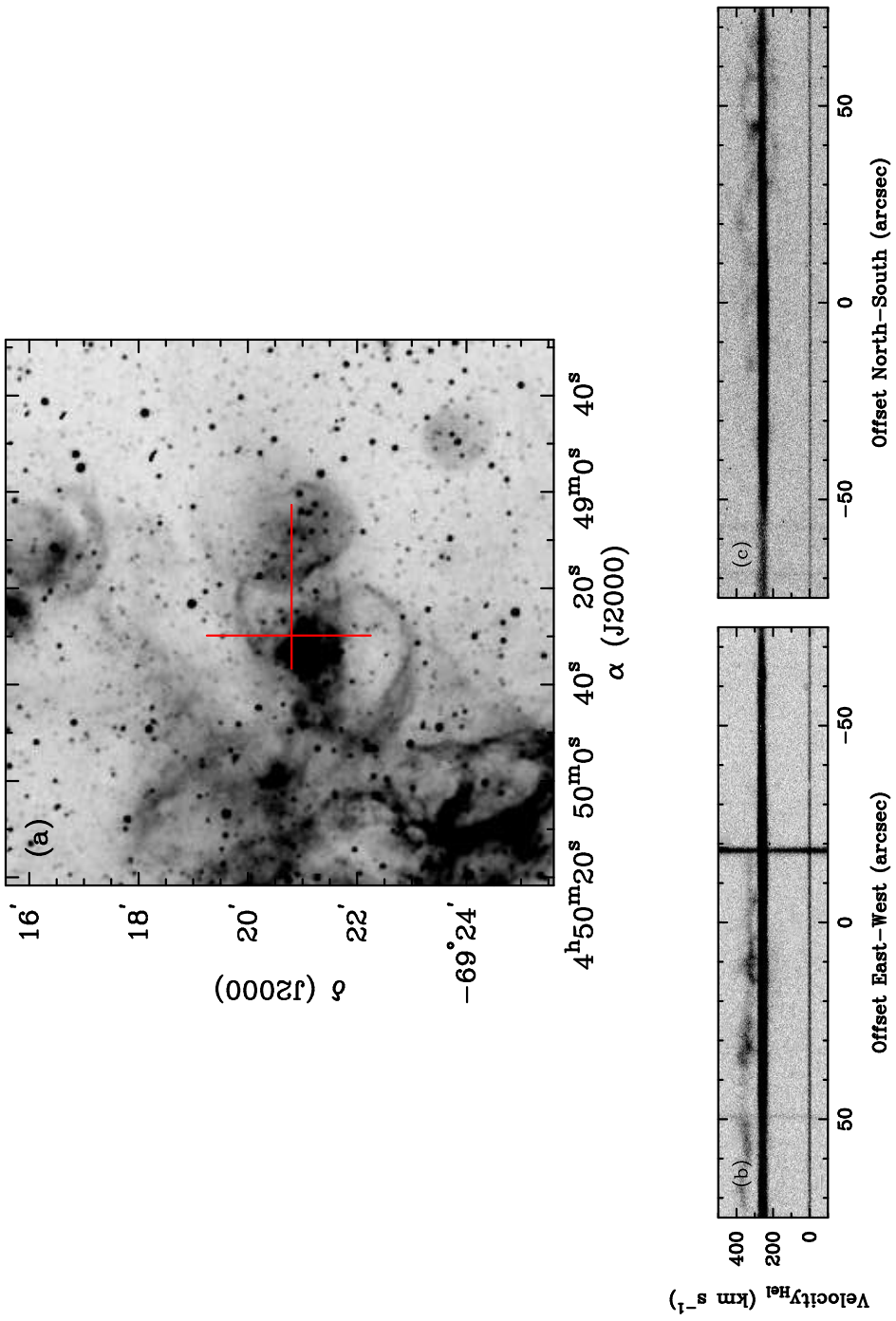

Fig. 8.— Hα image of SNR0449−6921 showing slit position and resulting echelle spectrum.

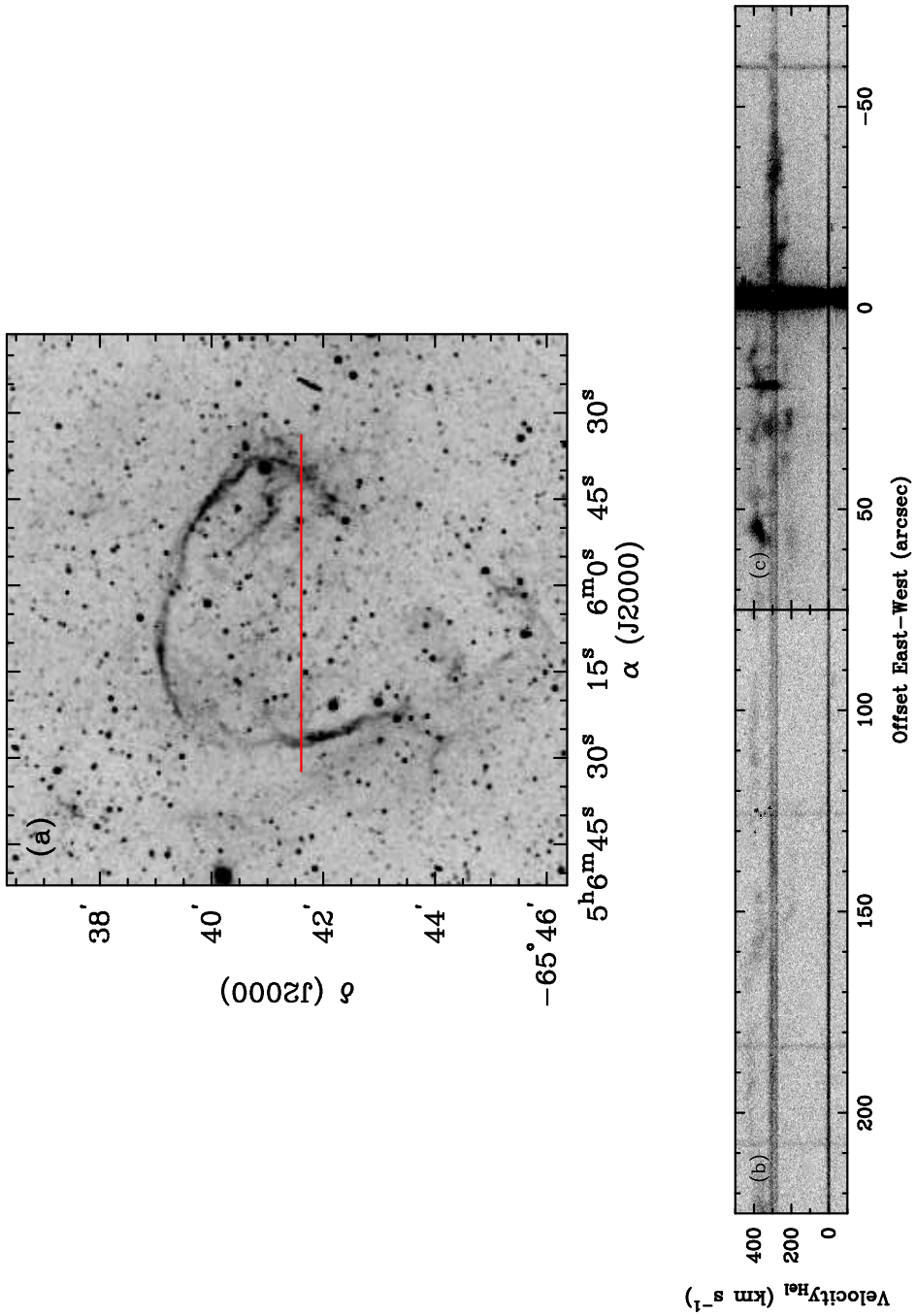

Fig. 9.— Hα image of SNR0506−6541 showing slit position and resulting echelle spectrum.

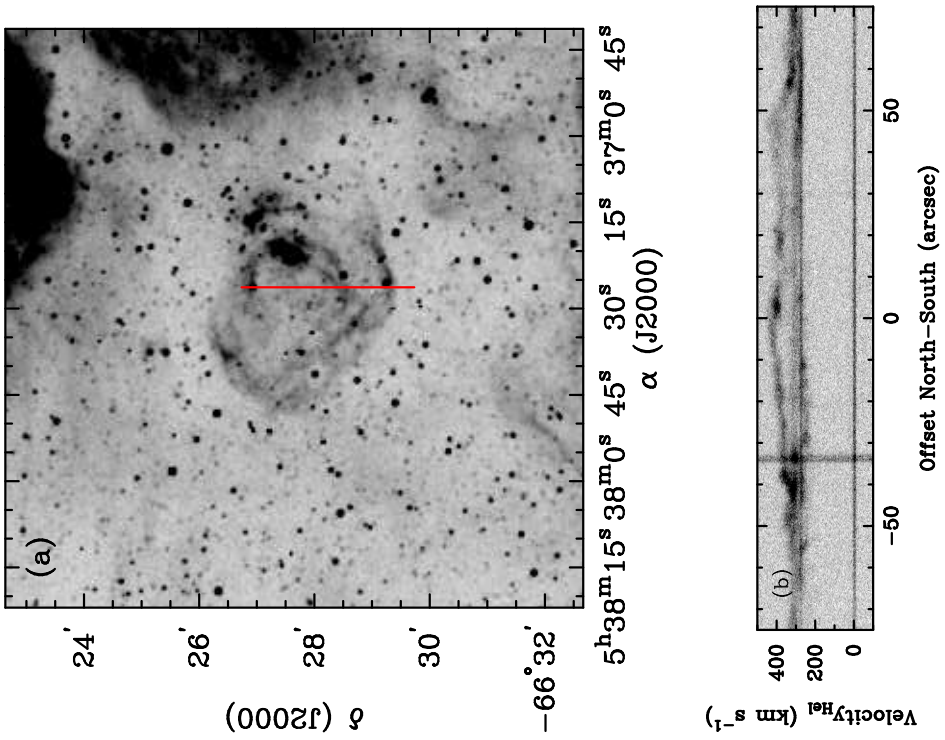

Fig. 10.— Hα image of SNR0537−6628 showing slit position and resulting echelle spectrum.

Table 1. Journal of MCELS Observations

Object	Field ID	Field Center R.A. (J2000)	Field Center Decl. (J2000)	Exposure (s) [O III]	Green	Hα	[S II]	Red	UT Date of Observation
MCELS SNR0449−6921	LMC [5,-2]	04 54 47	−69 15 00	2x600	2x300	2x300	2x600	2x300	1997 Nov 30
MCELS SNR0506−6541	LMC [3, 6]	05 04 04	−65 15 00	2x600	2x300	2x300	2x600	2x300	1997 Dec 04

Note. — Units of right ascension are hours, minutes, and seconds, and units of declination are degrees, arcminutes, and arcseconds.

Table 2. Journal of *XMM-Newton* Observations

		Field Center			
		R.A.	Decl.		UT Date of
Object	Field ID	(J2000)	(J2000)	Exposure	Observation

Table 3. Physical Properties of SNRs

	SNR0449−6921	SNR0506−6541	SNR0537−6628
R (pc)	15.45	37.15	23.4
SB (1×10^{-15})	0.9	0.5	0.4
v_{exp} (km s^{-1})	110	115	95
$n_{e,shell}$ (cm^{-3})	5.22	2.70	2.52
V_{shell} (cm^3)	1.79×10^{59}	1.90×10^{60}	9.34×10^{59}
M_{shell} ($M_\odot$)	997	5463	2510
K (erg)	1.20×10^{50}	7.18×10^{50}	2.25×10^{50}
P_{shell} (dyne cm^{-2})	1.44×10^{-11}	7.45×10^{-12}	6.95×10^{-12}
N_H (1×10^{22} cm^{-2})	0.55	0.56	0.25
kT (keV)	0.22	0.13	0.25
$n_{e,hot}$ (cm^{-3})	$0.29 f_{hot}^{-1/2}$	$0.13 f_{hot}^{-1/2}$	$0.09 f_{hot}^{-1/2}$
M_{hot} ($M_\odot$)	$129 f_{hot}^{1/2}$	$2752 f_{hot}^{1/2}$	$142 f_{hot}^{1/2}$
E_{th} (erg)	$1.36 \times 10^{50} f_{hot}^{1/2}$	$1.73 \times 10^{50} f_{hot}^{1/2}$	$1.64 \times 10^{50} f_{hot}^{1/2}$
P_{hot} (dyne cm^{-2})	$1.99 \times 10^{-10} f_{hot}^{-1/2}$	$1.82 \times 10^{-10} f_{hot}^{-1/2}$	$6.88 \times 10^{-11} f_{hot}^{-1/2}$
Age (yr)	4.54×10^4	1.04×10^5	7.95×10^4
environment	H II region	isolated	H II region